Pure Appl. Geophys.

https://doi.org/10.1007/s00024-018-02090-3

Pure and Applied Geophysics

Role of Lower Crust in the Postseismic Deformation of the 2010 Maule Earthquake: Insights from a Model with Power-Law Rheology

Carlos Peña,[1,2] Oliver Heidbach,[1] Marcos Moreno,[1,3] Jonathan Bedford,[1] Moritz Ziegler,[1,4] Andrés Tassara,[5,6] and Onno Oncken[1,2]

Abstract—The surface deformation associated with the 2010 M_w 8.8 Maule earthquake in Chile was recorded in great detail before, during and after the event. The high data quality of the continuous GPS (cGPS) observations has facilitated a number of studies that model the postseismic deformation signal with a combination of relocking, afterslip and viscoelastic relaxation using linear rheology for the upper mantle. Here, we investigate the impact of using linear Maxwell or power-law rheology with a 2D geomechanical-numerical model to better understand the relative importance of the different processes that control the postseismic deformation signal. Our model results reveal that, in particular, the modeled cumulative vertical postseismic deformation pattern in the near field (< 300 km from the trench) is very sensitive to the location of maximum afterslip and choice of rheology. In the model with power-law rheology, the afterslip maximum is located at 20–35 km rather than > 50 km depth as suggested in previous studies. The explanation for this difference is that in the model with power-law rheology the relaxation of coseismically imposed differential stresses occurs mainly in the lower crust. However, even though the model with power-law rheology probably has more potential to explain the vertical postseismic signal in the near field, the uncertainty of the applied temperature field is substantial, and this needs further investigations and improvements.

1. Introduction

At subduction zones, the sudden release of strain that has accumulated over tens to hundreds of years repeatedly produces the failure of large areas of the boundary interface, resulting in great ($M_w > 8.5$) or even giant ($M_w > 9.0$) earthquakes (Barrientos and Ward 1990; Chlieh et al. 2008; Moreno et al. 2012; Schurr et al. 2014). This sudden slip is followed by postseismic deformation that gradually relaxes the coseismically induced stress perturbations. The rate of postseismic deformation is time-dependent and has been attributed to three primary processes: (1) afterslip (Bedford et al. 2013; Hsu et al. 2006; Perfettini et al. 2010; Tsang et al. 2016), (2) poro-elastic rebound (Hu et al. 2014; Hughes et al. 2010) and (3) viscoelastic relaxation (Hu et al. 2004; Pollitz et al. 2006; Qiu et al. 2018; Rundle, 1978; Wang et al. 2012). Interseismic relocking or simply relocking is another process that may occur shortly after megathrust events. Bedford et al. (2016) inferred that the fault interface relocked within the first year after the 2010 Maule earthquake. A similar finding was obtained by Remy et al. (2016) after the 2007 Pisco, Peru, earthquake. In the past decade, the increased spatial density of continuous GPS (cGPS) instrumentation at subduction zones together with the implementation of geomechanical-numerical models has allowed us to test the relative importance of these processes in time and space (Bedford et al. 2016; Govers et al. 2017; Klein et al. 2016; Li et al. 2017; 2018; Sun et al. 2014). In these studies, linear viscoelastic relaxation has been used to infer the viscosity structure of the upper mantle and to understand the postseismic deformation signal in the

[1] Helmholtz Centre Potsdam, GFZ German Research Centre for Geosciences, Potsdam, Germany. E-mail: carlosp@gfz-potsdam.de
[2] Freie Universität Berlin, Berlin, Germany.
[3] Departamento de Geofísica, Universidad de Concepción, Concepción, Chile.
[4] Institute of Earth and Environmental Science, University of Potsdam, Potsdam, Germany.
[5] Departmento de Ciencias de la Tierra, Universidad de Concepción, Concepción, Chile.
[6] Millenium Nucleus CYCLO “The Seismic Cycle along Subduction Zones”, Valdivia, Chile.

Published online: 22 January 2019

Birkhäuser

near, middle and far field. These models assume that the crust is purely elastic and that the relaxation in the upper mantle can be described with a linear viscoelastic rheology using either the Maxwell (Govers et al. 2017; Hu et al. 2004; Li et al. 2017, 2018) or Burgers body (Klein et al. 2016; Sun et al. 2014). Furthermore, most of these models consider an inversion scheme to estimate the location and magnitude of afterslip as well as the viscosity structure of the mantle that results in a best fit of the observed cumulative postseismic deformation signal derived from GPS observations. Alternatively, in their 2D geomechanical-numerical forward model Hergert and Heidbach (2006) showed that a power-law rheology with dislocation creep can also fit the vertical and horizontal time series of the postseismic relaxation after the 2001 Arequipa earthquake. However, for their study only one cGPS station at 225 km distance from the trench was available and no afterslip was considered.

The 2010 M_w 8.8 Maule earthquake that struck south-central Chile was one of the first great events to be captured by modern space-geodetic monitoring networks (Vigny et al. 2011; Moreno et al. 2012). Through a rapid international collaborative effort, a dense cGPS network of 67 stations (Bedford et al. 2013; Bevis et al. 2010; Vigny et al. 2011) was installed to monitor the postseismic surface deformation (Fig. 1). Recent analyses of the postseismic deformation signal from the Maule earthquake have drawn attention to the limits posed by using a linear viscoelastic relaxation with homogeneous viscosity distribution in the mantle (Klein et al. 2016; Li et al. 2017, 2018) to explain the heterogeneity of the vertical postseismic signal, showing that a simple process is not a candidate to explain the postseismic signal associated with the 2010 Maule case. The best-fit model from Klein et al. (2016) results in a heterogeneous viscosity structure with a deep viscoelastic channel up to 135 km depth along the fault interface and afterslip at regions close to the up- and down-dip limits to explain in particular the pattern of the observed vertical displacement and the displacement over time in the north, east and vertical components recorded by the cGPS time series. On the other hand, Li et al. (2017, 2018) showed how lateral viscosity variations improve the fit of the observed cumulative postseismic vertical deformation while having less effect on the horizontal predictions. Furthermore, they speculate that a power-law rheology could also explain the postseismic relaxation, in agreement with results from laboratory experiments (Bürgmann and Dresen 2008; Hirth and Tullis 1992; Karato and Wu 1993; Kirby and Kronenberg 1987).

In this article, we investigate the general differences that result from the use of a power-law rheology compared with a linear viscoelastic relaxation in a Maxwell body for the purpose of better understanding the processes controlling the spatio-temporal patterns of the postseismic deformation signal. We construct a 2D geomechanical-numerical model along a cross section perpendicular to the strike of the subduction zone at 36°S sub-parallel to the maximum of the coseismic slip of the Maule earthquake (Fig. 1). We model the first 6 years of postseismic deformation and compare our model results with the vertical and horizontal components of the cumulative and time series displacements of cGPS sites as a function of distance from the trench. The primary focus of this study is not to achieve a best-fit solution of the cGPS signal using an inversion scheme; instead, we use forward models to study the principal differences between a linear Maxwell and power-law rheology. However, the results of our test series to study the sensitivity due to linear Maxwell versus power-law rheology as well as due to the location and magnitude of afterslip partly show a remarkably good fit to the observed postseismic signals.

Our model results indicate that the overall contribution of relocking to the cumulative postseismic deformation signal is small compared with the impact of afterslip and viscoelastic relaxation. Our model results confirm previous studies (Klein et al. 2016; Li et al. 2017, 2018; Qiu et al. 2018) that showed that the vertical postseismic deformation signal is the key to better assess the relative importance of the involved processes, i.e., the viscosity, effective viscosity, maximum magnitude and location of afterslip. We show that in particular the predicted cumulative vertical postseismic signal in the near field (distance < 300 km from the trench) is very sensitive to the choice of model rheology as well as the afterslip location and maximum. The model with power-law

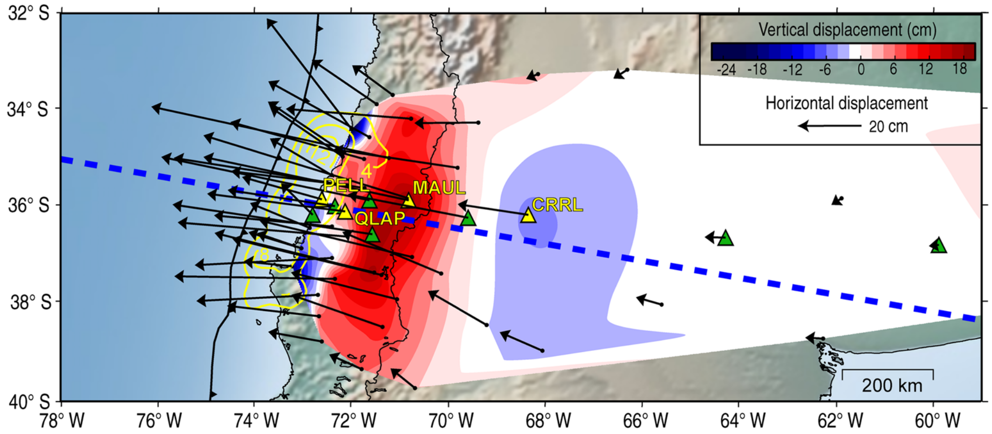

Figure 1
Study area and cumulative postseismic displacement after 6 years of the Maule event derived from cGPS observations in the stable South American reference frame. Horizontal (black arrows) and interpolated vertical displacements (color coded) show the cumulative postseismic deformation in the first 6 years after the M_w 8.8 Maule earthquake. Green and yellow triangles display the 11 cGPS sites used in this study. Yellow triangles show the four cGPS sites considered for the time series analysis. Yellow contour lines depict the 2010 Maule earthquake coseismic slip from Moreno et al. (2012). Blue dotted line represents the 2D model cross section oriented parallel to the horizontal postseismic deformation

rheology favors afterslip at depths of 20–35 km rather than at the down-dip limit of the seismogenic zone > 50 km. This shift of afterslip location is explained with the dislocation creep process that occurs in the deeper part of the lower crust and the uppermost mantle.

2. *Model Description*

2.1. *Model Setup*

In the first 6 years following the Maule event, the postseismic surface displacement is almost perpendicular to the strike of the trench. We thus choose a 2D model cross section oriented parallel to the direction of the observed horizontal cumulative postseismic displacement vector. The model geometry is derived from the model of Li et al. (2017). The cross section is almost perpendicular to the trench and cuts through the center of the coseismic rupture where the key postseismic deformation processes take place (Fig. 1). The model geometry takes into account the geometry of the slab (Hayes et al. 2012) and extends 3800 km in the horizontal and 400 km in the vertical direction to avoid boundary effects (Fig. 2a).

The model is discretized with 112,000 finite elements with a high resolution close to the slab interface where the coseismic displacement occurs and a significantly coarser resolution at the model boundaries where no deformation is expected. We assign to each element the rock properties presented in Table 1 differentiating the continental crust, oceanic crust/slab and upper mantle. At the lower and lateral model boundaries, the model cannot displace in the normal direction, but it is free to move parallel to the model boundaries; the model surface is free of constraints (Fig. 2a).

The temperature field of the model is taken from Springer (1999) by interpolating the temperature contours and assigning the according temperature to each node of the finite elements (Fig. 2b). The temperature field is assumed to be time-independent as no significant changes are expected within 6 years. Coseismic slip models for the Maule earthquake (Bedford et al. 2013; Klein et al. 2016; Moreno et al. 2012; Vigny et al. 2011; Yue et al. 2014) show some differences, mainly in magnitude and location of maximum slip. This is most probably due to the use of different data sets and regularization methods in the inversion process. Postseismic deformation modeled with power-law rheology depends on the

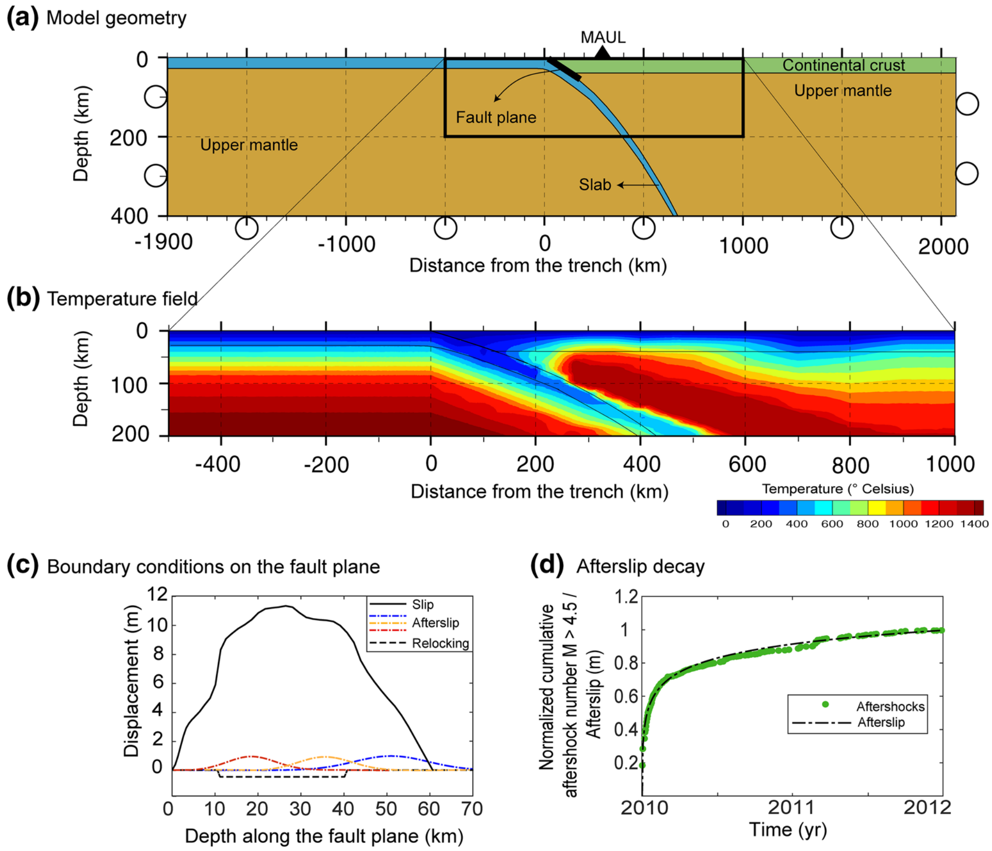

Figure 2

Model setup. **a** The 2D model geometry along the cross section is shown in Fig. 1. Circles indicate that no displacement is allowed perpendicular to the model boundary. **a** Exaggerated in the vertical by a factor of two. **b** The implemented temperature field according to Springer (1999) in the area of key interest. **c** Distribution of coseismic slip taken from the inversion of Moreno et al. (2012) and afterslip distributions. **d** Afterslip decay law used in this study. The aftershocks seismicity corresponds to $M_w > 4.5$ taken from the NEIC catalogue (http://www.usgs.gov)

Table 1

Elastic and creep parameters

Layer	Rock type[b]	Young's module E (MPa)[a]	Poisson's ratio v[a]	Pre-exponent A ($\mathrm{MPa}^{-n}\ \mathrm{s}^{-1}$)[b]	Stress exponent n[b]	Activation enthalpy Q ($\mathrm{kJ\ mol}^{-1}$)[b]
Continental crust	Wet quartzite	1×10^5	0.265	3.2×10^{-4}	2.3	154
Oceanic crust/slab	Diabase	1.2×10^5	0.3	2.0×10^{-4}	3.4	260
Upper mantle	Olivine	1.6×10^5	0.25	2.0	3.0	433

[a]Reference source from Christensen (1996) and Khazaradze et al. (2002)

[b]Reference source from Ranalli (1997) and Karato and Wu (1993)

coseismic stress changes, and therefore may vary depending on the coseismic slip distribution. In this study, we decided to implement the coseismic slip distribution from the inversion of Moreno et al. (2012) as a displacement boundary condition on the fault plane (Fig. 2c), because our study shares the same numerical approach (FEM), margin geometry (slab and Moho discontinuities) and elastic material parameters as Moreno et al. (2012). To fit the observed coseismic displacement from previous studies (Moreno et al. 2012; Vigny et al. 2011), we assign 70% of the coseismic slip to the upper side of the fault plane toward the up-dip direction and 30% to the bottom side toward the down-dip direction (Govers et al. 2017; Hergert and Heidbach 2006; Sun and Wang 2015). The same ratio is applied to simulate afterslip and relocking.

The afterslip is modeled with a Gaussian distribution curve and decays exponentially to the 2nd year as explained by Marone et al. (1991). The afterslip decay law also is in agreement with the aftershock seismicity (Fig. 2d), which is a first-order approximation for the afterslip decay law for the 2010 Maule case (Bedford et al. 2016; Lange et al. 2014). Klein et al. (2016) found cumulated afterslip values on the order of 100 cm at 45 km depth between 2011 and 2012 for the postseismic deformation associated with the Maule event. Thus, we start with 100 cm of maximum afterslip centered at 48 km depth, but vary these values in different model scenarios. Different afterslip decay laws may achieve a better fit to the data; however, we do not explore this parameter since the main focus of this study is to investigate the first-order differences between the models that use linear Maxwell or power-law rheology instead of perfectly fitting the observations. Relocking is assumed as backslip on the rupture plane with a convergence velocity of 6 cm year^{-1} and takes place linearly up to the 6th year. With these kinematic boundary conditions, i.e., the coseismic rupture, afterslip distribution and relocking, the model simulates the postseismic relaxation of stresses during 6 years. The resulting numerical problem is solved using the commercial finite element code ABAQUS™, version 6.11.

2.2. Model Rheology

We implement the dislocation creep law for models with power-law rheology using the expression stated in Kirby and Kronenberg (1987)

$$\dot{\varepsilon} = A\sigma^n \exp\left(\frac{-Q}{RT}\right), \tag{1}$$

where $\dot{\varepsilon}$ is the strain rate, A is a pre-exponent parameter, σ the differential stress, n the stress exponent, Q the activation enthalpy for creep, R the gas constant and T the absolute temperature. The key control is the stress exponent n and the temperature field. In particular, the latter controls were in the continental crust where the brittle-ductile transition (BDT) zone is located (Brace and Kohlstedt 1980; Ranalli 1997). Below the BDT the differential stress is relaxed by dislocation creep processes. Our models with linear Maxwell rheology use a viscosity of 1.3×10^{19} Pa s for the uppermost mantle and elastic parameters for the crust and oceanic/slab. This value is in agreement with previous studies on the Chilean subduction zone (Bedford et al. 2016; Hu et al. 2004) that found viscosity values on the order of 10^{19} Pa s. We emphasize that the main difference is the fact that in our model with linear Maxwell rheology the whole crust is considered as an elastic material above a viscous mantle, while in the model with power-law rheology the viscosity distribution is controlled by the implemented temperature field. Elastic and creep parameters used in the model area are listed in Table 1.

2.3. GPS Observations

The cGPS observations in the Maule region show trench-ward motion in the horizontal component and different patterns of deformation in the vertical component along longitude, with a pronounced uplift in the Andean region (Fig. 1). We use the first 6 years of postseismic surface displacements observed by cGPS as reported by Li et al. (2017). In this data set, the effect of aftershocks was removed by applying the trajectory model of Bevis and Brown (2014). To compare with the prediction of our 2D model, we selected 11 cGPS sites distributed in the near, middle and far field for comparison with our model (yellow triangles in Fig. 1).

3. Results

Based on the model described in the previous section, we set up three different model groups to test the general difference when using linear Maxwell or power-law rheology in the model. An overview of different model parameters is provided in Table 2. In the first test group we focus on models with power-law rheology and investigate the relative impact of relocking and afterslip on the postseismic deformation pattern (Sect. 3.1 and Fig. 3). In the second test

Table 2

Description of the model parameters (rheology, afterslip and relocking) used in this study

Model	Maximum of afterslip (cm)	Depth of maximum afterslip (km)	Relocking (cm year^{-1})	Temperature (°C)	Graph color and type
NLA100D48R	100	48	6	T	Figures 3, 4 and 5: solid blue
NLA100D35R	100	35	6	T	Figure 5: solid orange
NLA100D20R	100	20	6	T	Figures 5 and 6: solid red
NLA100D48	100	48	–	T	Figure 3: solid thin blue
NLA20D48R	20	48	6	T	Figures 3 and 4: solid cyan
NLA20D48	20	48	–	T	Figure 3: solid thin cyan
NLA0R	0	–	6	T	Figures 3 and 4: solid green
NLA0	0	–	–	T	Figures 3, 6 and 8: solid thin green
NLA0T + 100	0	–	–	T + 100	Figure 8: solid dark red
NLA0T-100	0	–	–	T − 100	Figure 8: solid pink
LA100D48R	100	48	6	T	Figures 4 and 5: dashed blue
LA100D35R	100	35	6	T	Figure 5: dashed orange
LA100D20R	100	20	6	T	Figures 5 and 6: dashed red
LA20D48R	20	48	6	T	Figure 4: dashed cyan
LA0R	0	–	6	T	Figure 4: dashed green
LA0	0	–	–	T	Figure 6: dashed pink

The rheology, linear (L, Maxwell) and non-linear (NL, power-law), maximum afterslip (A), relocking (R) and changes in the initial temperature field from the Springer model (T) are indicated in the model name. If relocking is considered, it is always with a rate of 6 cm year^{-1}

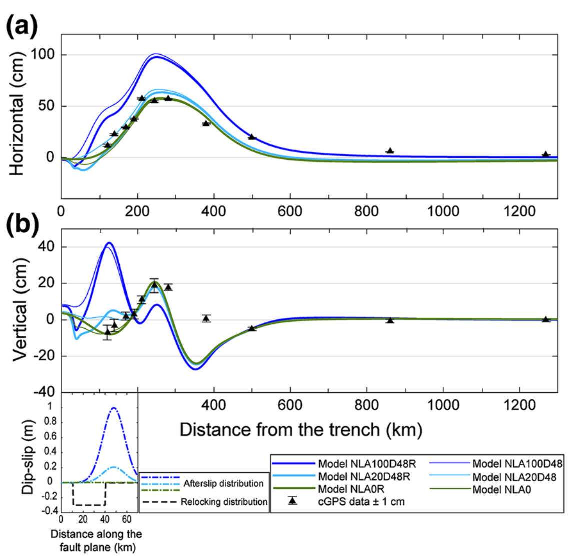

Figure 3

Relative impact of afterslip and relocking for the cumulative surface displacement 6 years after the Maule event compared with cGPS observations. Afterslip and relocking distributions for the six models are shown below the figures at the location relative to the trench. **a** Horizontal displacement: positive values represent trenchward motion and negative landward motion. cGPS displacements are projected onto the model cross section. **b** Vertical displacement

group we focus on differences when using linear Maxwell or power-law model rheology and different afterslip magnitudes (Sect. 3.2 and Fig. 4), and in the third test group we investigate the differences when using linear Maxwell or power-law model rheology and different depth locations of the maximum afterslip (Sect. 3.3 and Fig. 5).

3.1. Relative Impact of Relocking and Afterslip in Models with Power-Law Rheology

Figure 3 shows the comparison of the cumulative postseismic surface displacement after 6 years between the model results and the data from the cGPS stations. We used three different maximum amplitudes of afterslip at 48 km depth. To evaluate the relative contribution of relocking, we fully and uniformly locked the fault interface as backslip between 10 and 40 km depth (Govers et al. 2017; Tichelaar and Ruff 1993). We also perform tests without relocking to assess its relative impact on the cumulative vertical and horizontal postseismic displacement signal (Fig. 3). The models with and without relocking produce landward motion in the

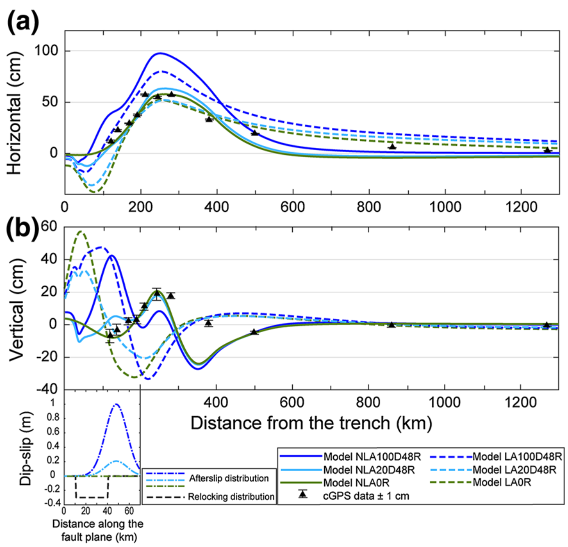

Figure 4
Impact of rheology and afterslip maximum on the cumulative surface displacement 6 years after the Maule earthquake compared with cGPS observations. Afterslip and relocking distributions for the six models are shown below the figures at the location relative to the trench. **a** Horizontal displacement. GPS velocities are projected onto the model cross section. **b** Vertical displacement

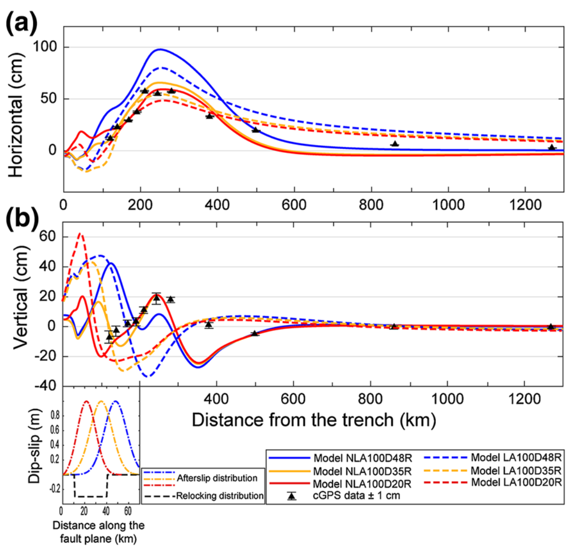

Figure 5
Impact of rheology and location of the afterslip maximum on the cumulative surface displacement 6 years after the Maule earthquake compared with cGPS observations. Afterslip and relocking distributions for the six models are shown below the figures at the location relative to the trench. **a** Horizontal displacement. GPS velocities are projected onto the model cross section. **b** Vertical displacement

very near field (< 50 km from the trench). In general, our results indicate that relocking does not affect the deformation field significantly (see continuous versus dashed lines in Fig. 3). A small signal is seen close to the trench (< 80 km from the trench), and it vanishes at distances > 200 km from the trench for both the horizontal and vertical displacements. Changing the maximum of the afterslip does not change the pattern of the horizontal surface deformation at distances > 600 km from the trench, but it changes the magnitude of trench-ward motion at distances between 150 and 400 km from the trench. Beyond distances of 600 km from the trench, the results show trench-ward motion when 100 cm of maximum afterslip is used, but small landward motion when it is reduced to 20 and 0 cm, respectively. Interestingly, our results show that the vertical deformation is the component most sensitive to the afterslip maximum. The afterslip centered at the down-dip limit of the seismogenic zone produces maximum uplift around 100 km from the trench. When 100 cm afterslip is applied, an uplift of 40 cm after 6 years is accumulated. This number is considerably reduced when only 20 cm maximum afterslip is used; without any afterslip it changes to subsidence. These results are in agreement with Wang and Fialko (2014, 2018), who found afterslip at the down-dip limit produces uplift at that region, while subsidence is controlled by viscoelastic relaxation. Beyond distances of 400 km, the impact of different afterslip magnitudes is negligible.

The overall pattern of the horizontal cGPS signal is better explained by models with small afterslip at the down-dip limit of the seismogenic zone than when 100 cm of afterslip is considered, in particular in the area of largest deformation between 200 and 400 km from the trench. An increase in maximum afterslip results in an increase in surface deformation that leads to an overestimation of the horizontal component in the near field.

The observed patterns in the vertical signal are also in better agreement with models when a smaller afterslip is applied. Adding afterslip shifts the higher uplift signal toward the trench in a different pattern, as observed by the cGPS observations. All models are in a good agreement with the cGPS observations in the far field (> 500 km from the trench). However, none of the models can explain the wavelength of the declining uplift signal observed between 300 and 500 km from the trench (Fig. 3b). In general, the geomechanical-numerical model with power-law rheology results qualitatively in a good fit to the overall surface deformation pattern observed at the cGPS sites.

3.2. Impact of Afterslip Maximum in Models with Linear Maxwell and Power-Law Rheology

In the second model group, we model the cumulative surface deformation 6 years after the 2010 Maule event using models with linear Maxwell or power-law rheology and different afterslip magnitudes of 100, 20 and 0 cm located at the down-dip limit of the seismogenic zone (Fig. 4). We use the same three models with power-law rheology (as in Fig. 3), where the afterslip maximum is at 48 km depth, and compare these with models that have the same setup, but considering linear Maxwell rheology. Furthermore, despite the results presented in Fig. 3 that show a minor contribution from relocking on the cumulative surface deformation, in Fig. 4 we consider all models with relocking after 2 years.

Similar to the results presented in Sect. 3.1, the maximum of the afterslip also has an impact on the horizontal and vertical deformation signal for the models with linear Maxwell rheology, but it is smaller than the magnitude inferred using the models with power-law rheology, in particular for the vertical component (Fig. 4b). The horizontal component shows the largest differences between models with linear Maxwell and power-law rheology in amplitude and patterns in the near field among the models, but the difference in the overall pattern is small (Fig. 4a). In the far field all models with linear Maxwell rheology overestimate the horizontal displacement compared with the ones with power-law rheology. Significant differences between the models with linear and non-linear rheology are found in particular in the near field for the vertical component and to a lesser extent in the middle and far field (Fig. 4b). While models with power-law rheology show uplift at about 200–300 km and subsidence at about 300–700 km from the trench, models with linear rheology show the opposite surface displacement pattern.

Compared with the horizontal cGPS signal, the overall pattern from the models with linear Maxwell and power-law rheology agrees with the observations equally well in the area of key postseismic deformation, in the Andean region (Fig. 4a). However, for the vertical cGPS signal the models with linear Maxwell rheology reveal larger differences from the observed patterns than models with power-law rheology. This holds especially for the area 150–300 km from the trench.

3.3. Impact of Afterslip Location on Models with Linear Maxwell and Power-Law Rheology

In the third model group we shift the location of the maximum afterslip of 100 cm from 48 to 35 km and 20 km depth to investigate the impact on the surface deformation in models with linear Maxwell and power-law rheology. The choice of the maximum afterslip location has important effects on the surface deformation. In particular, for the horizontal component, models with linear Maxwell or power-law rheology and shallow afterslip result in a larger surface deformation than those using moderate deep afterslip for distances closer to 100 km from the trench (Fig. 5a). Beyond distances of 200 km from the trench, the surface deformation is smaller as shallow afterslip takes place, and it is also in the same fashion as the results from models without afterslip. These differences also apply to the vertical component, mainly in models with power-law rheology (Fig. 5b). For models with power-law rheology, the impact is much larger for distances closer to 200 km from the trench than the effect observed in the horizontal component. There, the differences are both in magnitude and patterns. This effect is less pronounced in models with linear Maxwell rheology. These models show a similar pattern of deformation, where the maximum uplift and subsidence are shifted around 40 km toward the trench as afterslip moves to closer distances from the trench on the fault plane.

The different patterns of deformation shown by these models can be compared with the cGPS signal to evaluate the relative impact of afterslip on the surface deformation signal. From models with power-law rheology, our results indicate that they can better explain the overall pattern observed by cGPS where shallow afterslip is considered. In particular, the vertical component gives clear insight to evaluate the relative impact of afterslip location for surface regions closer to 300 km from the trench. Here, the remarkable uplift at about 250 km and small subsidence at about 140 km from the trench can be just explained by the power-law rheology model with maximum afterslip at either 35 km or 20 km depth. None of these models result in very small uplift as shown by one cGPS site about 400 km from the trench. However, beyond these distances, power-law rheology models explain the cGPS displacement pattern.

In summary, the key findings from previous sections are: (1) relocking is not contributing significantly to the cumulative postseismic deformation signal along the chosen model profile; (2) models with linear Maxwell rheology without adaptation of the viscosity structure at depth fail to reproduce the pattern of the observed cumulative vertical postseismic deformation signal regardless of where the maximum afterslip is located and the amplitude of the afterslip; finally, (c) the general patterns of the cGPS observations are better explained by models with power-law rheology when small values of afterslip at the down-dip limit are considered and/or when afterslip is occurring at shallower regions.

3.4. *Model Results Versus Time Series of the cGPS Stations*

In this section we analyze the time series for 6 years after the Maule earthquake from four cGPS stations at different distances from the trench and compare these with the models with linear Maxwell and power-law rheology (Fig. 6). For this comparison we choose the models with 100 cm maximum afterslip at a depth of 20 km and 0 cm afterslip (Fig. 6). We selected the cGPS time series of the stations PELL, QLAP, MAUL and CRRL for comparison, which are located in the near, middle and far field (yellow triangles in Fig. 1) at about 130 km, 190 km, 270 km and 500 km distance from the trench, respectively.

The largest differences from models with and without afterslip are found in the near field (cGPS site PELL). As expected, models with afterslip (NLA100D20R and LA100D20R for the power-law and linear Maxwell case, respectively) result in larger deformation than when afterslip is assumed to be zero in particular in the near field. It is also observed that for the two cGPS sites at larger distance from the trench (MAUL and CRRL), the power-law rheology models with afterslip have very close deformation patterns and magnitudes but linear Maxwell rheology models keep small differences after 6 years. For sites at 190 km and 270 km from the trench, models with linear Maxwell and power-law rheology show very similar surface cumulative deformation for the horizontal component; however, there are large differences in the early part of the postseismic phase. In this period, the transient deformation of models with power-law rheology is much faster than linear Maxwell model scenarios, especially at 270 km from the trench where the cGPS MAUL site is located.

By comparing with the cGPS PELL site in the near field, it can be shown that the effect of afterslip is larger than that of viscous relaxation, in agreement with previous studies (Bedford et al. 2013; Hsu et al. 2006). A combination of afterslip and viscous relaxation can resemble the deformation patterns, in particular in the first 2 years. However, after the 2nd year, the model with power-law rheology can better explain the observed horizontal and vertical postseismic deformation pattern than models with linear Maxwell rheology. Compared with cGPS sites further from the trench, our results indicate that the preferred model also is a combination of power-law rheology and afterslip for both the horizontal and vertical component. Even though the models with Maxwell rheology and afterslip can produce good agreement with the cumulative surface deformation signal, they cannot produce the transient deformation in the early postseismic phase, as observations show. In the far field, at the cGPS CRRL site, no model is in agreement with the early postseismic deformation during the first years for the horizontal component. The vertical component is in very good agreement with models considering power-law rheology. In general, compared with the selected cGPS sites, models with power-law rheology show a better agreement with the overall deformation pattern signal than models with linear Maxwell rheology.

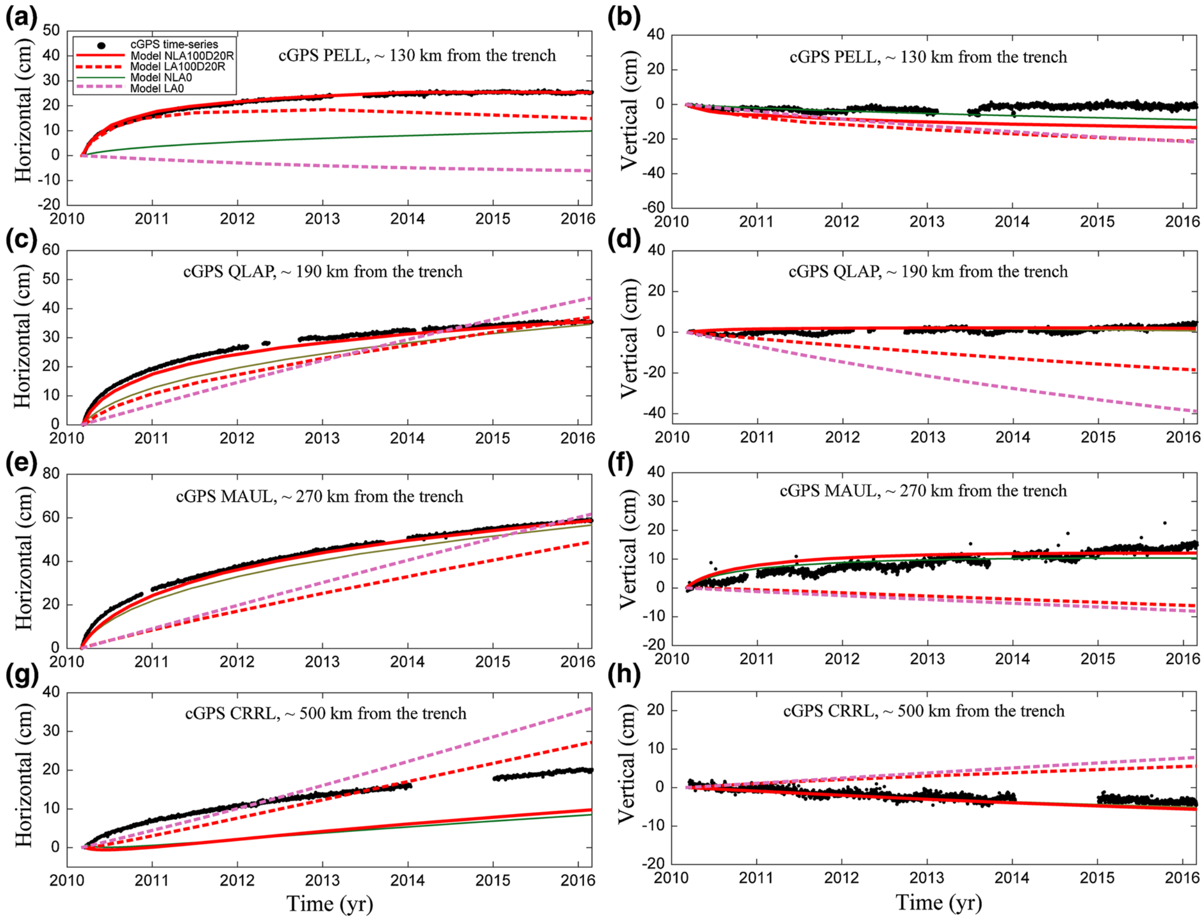

Figure 6

Time series of four cGPS stations versus model results from four models with linear Maxwell and power-law rheology for 6 years after the Maule event. Black dots are daily solutions of the cGPS observations; distance from the trench is given in km next to the station names. Left row (**a**, **c**, **e**, **g**) shows the horizontal displacement. GPS velocities are projected onto the model cross section. Right row (**b**, **d**, **f**, **h**) shows the vertical displacement

4. *Discussion*

4.1. Location of the Viscous Relaxation Process

The largest deformation for models with power-law rheology is produced in a region about 280 km landward from the trench (Fig. 7a). Interestingly, most of the viscoelastic relaxation occurs in the lower continental crust. This is in contrast to previous studies in the Chilean subduction zone, since these assumed that the whole crust is an elastic medium above a viscoelastic mantle (Hu et al. 2004; Klein et al. 2016; Li et al. 2017, 2018), resulting in relaxation mainly occurring in the mantle wedge, in agreement with our model results with linear Maxwell rheology (Fig. 7b).

Below the cGPS station MAUL, at 36 km depth, we infer a creep strain after 6 years of 7.9×10^{-5} and an effective viscosity of 1.1×10^{18} Pa s from the power-law model with 1 m of afterslip at 20 km depth. The creep strain and effective viscosity values are very similar for all models with power-law rheology. For the same region but at a shallower depth of only 10 km in the continental crust, we infer after 6 years a creep strain and effective viscosity on the order of 1×10^{-10} and 1×10^{22} Pa s, respectively. The model results using power-law rheology are in good agreement with a brittle upper crust and a

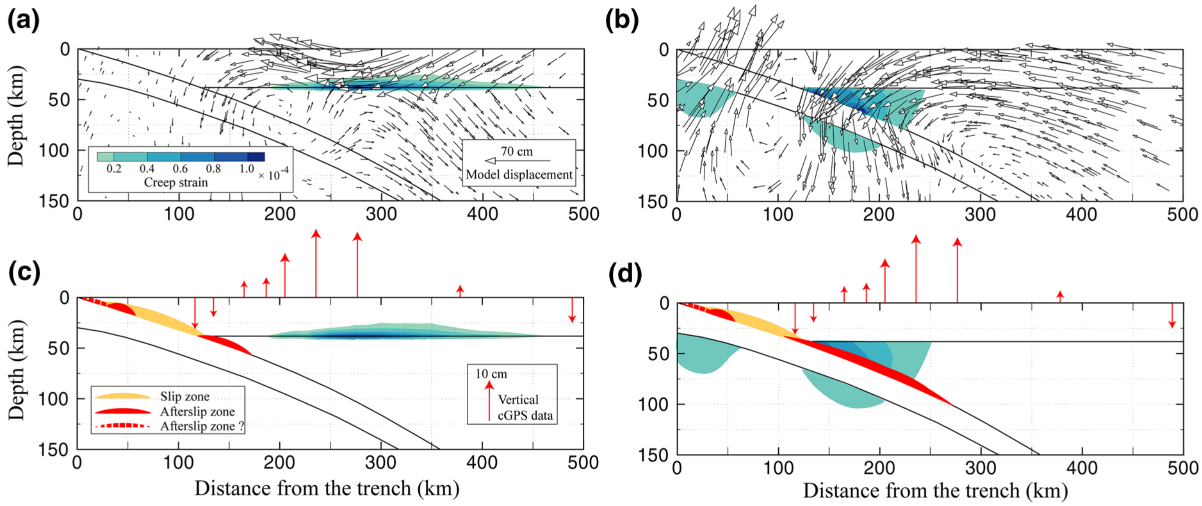

Figure 7

Modeled accumulated displacement field and creep strain 6 years after the Maule earthquake compared with the accumulated observed vertical displacement from nine cGPS stations along the model profile as shown in Fig. 1. **a** Modeled cumulative creep strain (second invariant of the creep strain tensor) and displacement vectors from model NLA0 (power-law rheology, no afterslip and no relocking). **b** Same as **a** but with linear model rheology (model LA0). **c** Schematic representation of where the afterslip occurs in case of the model shown in **a**. **d** Same as **c** using the linear Maxwell model rheology

ductile lower crust shown by laboratory extrapolation of the rock strength with depth (Brace and Kohlstedt 1980; Ranalli 1997). The high creep strain rate in the lower crust predicted by our model may be a result of the vertical geothermal gradient and rock composition at the boundary between the continental lower crust and the upper mantle. These results support the conclusion from Griggs and Blacic (1965) who raised the possibility of great stress relaxation in the deeper crust and uppermost mantle at temperatures far below the melting point. The latter is in agreement with other studies of postseismic relaxation that also consider rock viscosity below the solidus (Barbot 2018; Klein et al. 2016; Wang et al. 2012). Hence, this rheologic boundary likely affects geodetic observations of the postseismic deformation at the earth's surface.

4.2. *Implication of Linear Maxwell and Power-Law Model Rheology on Afterslip Location*

Uplift deformation observed by cGPS sites at distances between 200 and 300 km from the trench is also found for the postseismic deformation after the great 1960 Valdivia, Chile; 2011 Tohoku-Oki, Japan; great 2004 Sumatra-Andaman, Indonesia and 2015 Gorkha, Nepal, earthquakes (Hu et al. 2004; Muto et al. 2016; Qiu et al. 2018; Wang and Fialko 2018; Zhao et al. 2017), suggesting that postseismic surface deformation is driven by common relaxation processes. To explain this deformation pattern, our preferred model scenarios are those with power-law rheology and afterslip at the upper part of the fault plane (< 30 km depth) or at the down-dip limit less than 20 cm. Our model results suggest that such a remarkable uplift is mainly the result of stress relaxation in the lower crust due to dislocation creep (Fig. 7a), showing that afterslip in a deeper region of the megathrust fault plays a secondary role to explain the uplift pattern at those distances (Fig. 7c). The dislocation creep process occurs at distances relatively close to the surface; thus, the deformation produced by this process does not need to be high to explain this pattern. Previous studies showed that this pattern can be explained by using linear viscoelastic rheology in the uppermost mantle in combination with afterslip, especially at the down-dip limit at about 55 km depth or deeper regions (Govers et al. 2017; Klein et al. 2016; Noda et al. 2017; Yamagiwa et al. 2015). In the same fashion, our model results from linear Maxwell model rheology suggest that deeper afterslip is required to explain this pattern

(Fig. 7d). However, evidence from interseismic locking obtained from GPS velocities (Moreno et al. 2010) or friction laws (Scholz 1998) along megathrust faults suggests that below approximately 55 km depth the megathrust is probably fully unlocked and no strain is built up to be released as frictional slip after the earthquake. Such a deep aseismic slip may not be only due to frictional processes, but may also occur as strain localization within ductile shear zones. Montési and Hirth (2003) proposed a theoretical model to investigate the impact of dislocation and diffusion creep processes on the transient behavior of ductile shear zones considering grain size evolution. They found that a ductile shear zone resembles frictional afterslip on a deep extension of the fault. This result is also supported by Takeuchi and Fialko (2013). Nevertheless, they found that thermally activated shear zones have little effect of postseismic relaxation. Diffusion creep processes depend strongly on grain size evolution. Here, we have considered the dominance of dislocation creep over diffusion creep processes; therefore, we have not considered grain size evolution. However, further experiments are required to investigate its impact on postseismic deformation, in particular on ductile shear zones along the megathrust fault.

In the very near field ($<$ 50 km from the trench), our results show important differences in the cumulative surface displacement between models with linear Maxwell and power-law rheology, providing a key discriminant between the predominant rheology (linear or non-linear) and the magnitude and location of afterslip. Observations from the postseismic phase of the 2011 Tohoku-Oki earthquake indicated that the impact of afterslip is much smaller than was previously assumed when near-trench time series of GPS stations are used (Sun et al. 2014). Such stations observe a landward motion, which is not in agreement with substantial afterslip at the up-dip limit, which results in a seaward motion. Recently, Barbot (2018) used a power-law rheology in a 2D model to show that landward motion above the rupture area of the main shock can be produced by transient deformation in the oceanic asthenosphere. Our model with power-law rheology (Model LNA20D48R), in fact, results in a landward motion of $\sim$ 10 cm at 50 km distance from the trench, but since near-trench observations are missing in Chile, it remains a speculation whether landward motion would be observed or not.

4.3. *Uncertainties of the Temperature Field*

The largest uncertainty of the models with power-law rheology originates from the incorporated temperature model since this, besides the stress exponent, is the key control of the effective viscosity and thus the stress relaxation process induced by the coseismic slip and afterslip. Unfortunately, no temperature model exists for the entire cross section of the model, and we thus adopt the model from Springer (1999) that is located in the central Andes at 21°S. There, the age of the oceanic crust is older ($\sim$ 50 Ma) in contrast to the younger plate at 36°S ($\sim$ 35 Ma). Other temperature models closer to the Maule area (Oleskevich et al. 1999; Völker et al. 2011) only provide a temperature field 300 km landward from the trench not covering our model area. In contrast, the Springer model is covering the entire E–W extent of the modeled plate boundary system. Furthermore, Oleskevich et al. (1999) showed that in the fore arc and arc regions at 21°S and 34° the temperature contours have a very similar pattern, but absolute values can vary by 100 °C and more (Lamontagne and Ranalli 1996).

To show the model sensitivity due to the initial temperature field T, we increased (Model NLA0T + 100) and decreased (Model NLA0T − 100) the temperatures by 100 °C, respectively (Fig. 8). Since we would like to investigate only the impact of viscoelastic relaxation due to temperature changes on the deformation, we considered the model with power-law rheology and without afterslip. The results display a strong impact of the temperature field on the surface deformation, undergoing a maximum surface displacement change by a factor of about two, in the region of largest deformation at the Andean region (Fig. 8c, d). Thus, the mismatch of patterns of the slight uplift at about 350 km from the trench and the trench-ward motion in the far field ($>$ 570 km) shown by cGPS observations and our model results, but also obtaining the afterslip, might be due to the temperature uncertainties.

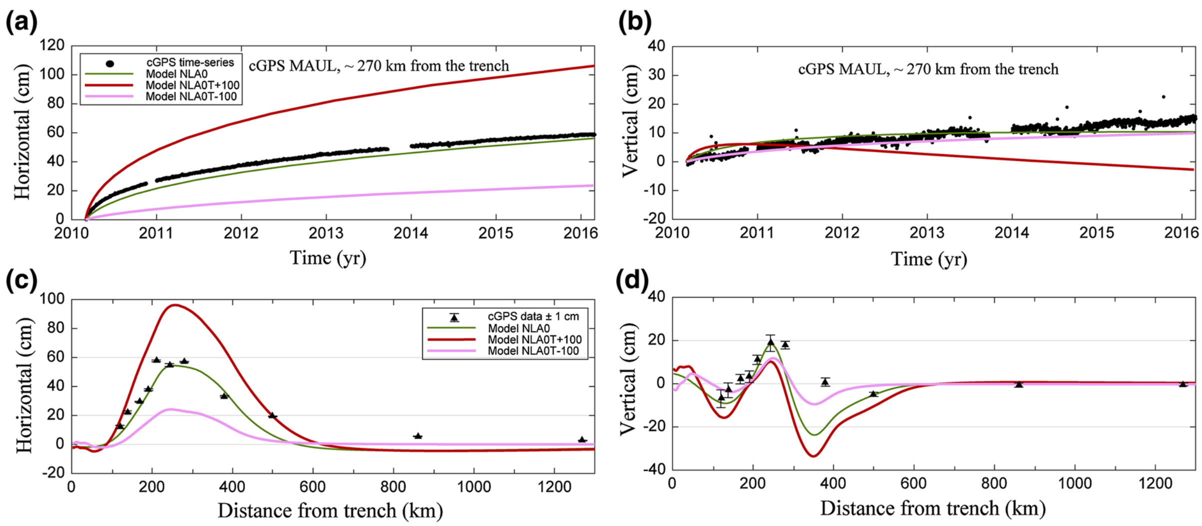

Figure 8

Results of the temperature sensitivity test for the model with power-law rheology. **a** Time series of the horizontal displacement of the cGPS station MAUL projected onto the model profile compared with model results for the temperature test. **b** Same as **a** for the vertical displacement. **c** Cumulative horizontal displacement of the cGPS stations indicated in Fig. 1 after 6 years compared with model results for the temperature test. **d** Same as **c** for the cumulative vertical displacement

5. *Conclusion*

We used a 2D geomechanical-numerical model to study the relative impact of afterslip, relocking and viscoelastic relaxation on the observed postseismic deformation 6 years after the 2010 Maule earthquake. In particular, we tested the general difference of using linear Maxwell or power-law rheology. The overall impact of relocking is only visible at distances < 200 km from the trench, but small compared with afterslip and viscoelastic relaxation. For the cumulative horizontal displacement the overall pattern from models with linear Maxwell and power-law rheology is similar. However, for the cumulative vertical displacement this is different. Here the used afterslip magnitudes as well as its depth location have a different expression in the modeled cumulative vertical displacement. To reproduce the pattern of the cGPS observations, the model with power-law rheology requires afterslip in shallower regions at 20–30 km depth rather than afterslip at depth > 50 km as suggested by models with linear rheology (Bedford et al. 2016; Klein et al. 2016). It also seems that less afterslip is needed at shallow depths. This difference is due to the different processes that are induced. In the models with power-law rheology the coseismically induced differential stresses in the lower crust and upper mantle are relaxed in shallower regions, i.e., the lower crust, whereas the models with linear Maxwell rheology assume that the crust is elastic. To produce the same vertical postseismic displacement these models require a relatively high afterslip at greater depth. To discriminate which model assumption is ultimately controlling the post-seismic relaxation processes, cGPS stations near the trench are needed, and these turning points between subsidence and uplift as well as the change in direction of the horizontal displacement toward or away from the trench could be used as a proxy for the location and amount of afterslip as well as for the depth where differential stresses are relaxed by linear or non-linear viscoelastic processes.

Acknowledgements

Carlos Peña appreciates the scholarship granted to him by both the German Academic Exchange Service (DAAD) and the National Commission for Scientific and Technological Research (CONICYT-Becas

Chile). Jonathan Bedford is grateful to the German Science Foundation (DFG, MO-2310/3-1). Marcos Moreno acknowledges support from the Chilean National Fund for Development of Science and Technology (FONDECYT) grants 1181479, Millennium Scientific Initiative (ICM) grant NC160025, and National Research Center for Integrated Natural Disaster Management (CIGIDEN), CONICYT/FONDAP/15110017. Andrés Tassara is grafetul to the National Fund for Scientific and Technological Development, FONDECYT 1151175. The authors thank Shaoyang Li for the discussion in the early stage of the manuscript. All data used are properly cited in the reference list, figures, and tables.

References

Barbot, S. (2018). Asthenosphere flow modulated by megathrust earthquake cycles. *Geophysical Research Letters*, *45*, 6018–6031. https://doi.org/10.1029/2018GL078197.

Barrientos, S., & Ward, S. (1990). The 1960 Chile earthquake: Inversion for slip distribution from surface deformation. *Geophysical Journal International, 103*(3), 589–598. https://doi.org/10.1111/j.1365-246X.1990.tb05673.x.

Bedford, J., Moreno, M., Baez, J. C., Lange, D., Tilmann, F., Rosenau, M., et al. (2013). A high-resolution, time-variable after slip model for the 2010 Maule $M_w = 8.8$, Chile megathrust earthquake. *Earth and Planetary Science Letters, 383,* 26–36. https://doi.org/10.1016/j.epsl.2013.09.020.

Bedford, J., Moreno, M., Li, S., Oncken, O., Baez, J. C., Bevis, M., et al. (2016). Separating rapid relocking, afterslip, and viscoelastic relaxation: An application of the postseismic straightening method to the Maule 2010 cGPS. *Journal of Geophysical Research Solid Earth, 121,* 7618–7638. https://doi.org/10.1002/2016JB013093.

Bevis, M., & Brown, A. (2014). Trayectory models and reference frames for crustal motion geodesy. *Journal of Geodynamics, 88*(3), 283–311.

Bevis, B.A., Brooks, M.G., Smalley, R., Baez, J.C., Parra, H., Kendrick, E.C., Foster, J.H., Blanco, M., Simons, M., Caccamise, I., Genrich, D.A., Sladen, J.F., Melnick, M., Moreno, D., Cimbaro, S., Ryder, I.M., Wang, K., Bataille, K., Cassasa, G., Klotz, A., Folguera, J., Tong, X., Sandwell, D.T. (2010). The 2010 (M 8.8) Maule, Chile Earthquake: an overview of the emergency geodetic response and some of its early findings. Presented at 2010 Fall Meeting, AGU, U21B–04, San Francisco, Calif., 13–17 Dec.

Brace, W. F., & Kohlstedt, D. L. (1980). Limits on lithospheric stress imposed by laboratory experiments. *Journal of Geophysical Research, 85*(B11), 6248–6252. https://doi.org/10.1029/JB085iB11p06248.

Bürgmann, R., & Dresen, G. (2008). Rheology of the lower crust and upper mantle: Evidence from rock mechanics, geodesy and field observations. *Annual Review of Earth Planetary Sciences., 36*(1), 531–567. https://doi.org/10.1146/annurev.earth.36.031207.124326.

Chlieh, M., Avouac, J., Sieh, K., Natawidjaja, D., & Galetzka, J. (2008). Heterogeneous coupling of the Sumatran megathrust constrained by geodetic and paleogeodetic measurements. *Journal of Geophysical Research, 113,* B5. https://doi.org/10.1029/2007JB004981.

Christensen, N. (1996). Poisson's ratio and crustal seismology. *Journal of Geophysical Research, 101*(B2), 3139–3156. https://doi.org/10.1029/95JB03446.

Govers, R., Furlong, K., van de Wiel, L., Herman, M., & Broerse, T. (2017). The geodetic signature of the earthquake cycle at subduction zones: Model constraints on the deep processes. *Reviews of Geophysics, 56*(1), 6–49. https://doi.org/10.1002/2017RG000586.

Griggs, D. T., & Blacic, D. J. (1965). Quartz: Anomalous weakness of synthetic crystals. *Siences, 147*(3755), 292–295. https://doi.org/10.1126/science.147.3655.292.

Hayes, G., Wald, D., & Johnson, R. (2012). Slab1.0: A three-dimensional model of global subduction zone geometries. *Journal of Geophysical Research Solid Earth, 117*(B1), B01302. https://doi.org/10.1029/2011JB008524.

Hergert, T., & Heidbach, O. (2006). New insights into the mechanism of the postseismic stress relaxation exemplified by the 23 June $M_w = 8.4$ earthquake in southern Peru. *Geophysical Research Letters, 30,* 02307. https://doi.org/10.1029/2005GL024858.

Hirth, G., & Tullis, J. (1992). Dislocation creep regimes in quartz aggregates. *Journal of Structural Geology, 14*(2), 145–159. https://doi.org/10.1016/0191-8141(92)90053-Y.

Hsu, Y. J., Simons, M., Avouac, J. P., Galeteka, J., Sieh, K., Chlieh, M., et al. (2006). Frictional afterslip following the 2005 Nias-Simeulue earthquake, Sumatra. *Science, 312*(5782), 1921–1926. https://doi.org/10.1126/science.1126960.

Hu, Y., Bürgmann, R., Freymueller, J., Banerjee, P., & Wang, K. (2014). Contributions of poroelastic rebound and a weak volcanic arc to the postseismic deformation of the 2011 Tohoku earthquake. *Earth Planets and Space, 66*(1), 106. https://doi.org/10.1186/1880-5981-66-106.

Hu, Y., Wang, K., He, J., Klotz, J., & Khazaradze, G. (2004). Three-dimensional viscoelastic finite element model for post-seismic deformation of the great 1960 Chile earthquake. *Journal of Geophysical Research, 109*(B12), B12403. https://doi.org/10.1029/2004JB003163.

Hughes, K., Masterlark, T., & Mooney, W. (2010). Poroelastic stress-triggering of the 2005 M8.7 Nias earthquake by the 2004 M9.2 Sumatra-Andaman earthquake. *Earth and Planetary Science Letters, 293*(3–4), 289–299. https://doi.org/10.1016/j.epsl.2010.02.043.

Karato, S., & Wu, P. (1993). Rheology of the upper mantle: A synthesis. *Science, 260,* 771–778. https://doi.org/10.1126/science.260.5109.771.

Kirby, S., & Kronenberg, A. (1987). Rheology of the lithosphere: Selected topics. *Reviews of Geophysics, 25,* 1219–1244. https://doi.org/10.1029/RG025i006p01219.

Klein, E., Fleitout, L., Vigny, C., & Garaud, J. D. (2016). Afterslip and viscoelastic relaxation model inferred from the large-scale postseismic deformation following the 2010 M_w 8.8 Maule earthquake (Chile). *Geophysical Journal International, 205*(3), 1455–1472. https://doi.org/10.1093/gji/ggw086.

Lamontagne, M., & Ranalli, G. (1996). Thermal and rheological constraints on the earthquake depth distribution in the Charlevoix, Canada, intraplate seismic zone. *Tectonophysics, 257*(1), 55–69. https://doi.org/10.1016/0040-1951(95)00120-4.

Lange, D., Bedford, J., Moreno, M., Tilmann, F., Baez, J., Bevis, M., et al. (2014). Comparison of postseismic afterslip models with aftershock seismicity for three subduction-zone earthquakes: Nias 2005, Maule 2010 and Tohoku 2011. *Geophysical Journal International, 199*(2), 784–799. https://doi.org/10.1093/gji/ggu292.

Li, S., Bedford, J., Moreno, M., Barnhart, W. D., Rosenau, M., & Oncken, O. (2018). Spatiotemporal variation of mantle viscosity and the presence of cratonic mantle inferred from 8 years of postseismic deformation following the 2010 Maule, Chile, earthquake. *Geochemistry Geophysics Geosystems*. https://doi.org/10.1029/2018GC007645.

Li, S., Moreno, M., Bedford, J., Rosenau, M., Heidbach, O., Melnick, D., et al. (2017). Postseismic uplift of the Andes following the 2010 Maule earthquake: Implications for the mantle rheology. *Geophysical Research Letters, 44*(4), 1768–1776. https://doi.org/10.1002/2016GL071995.

Marone, C., Scholtz, C., & Bilham, R. (1991). On the mechanics of earthquake afterslip. *Journal of Geophysical Research, 96*(B5), 8441. https://doi.org/10.1029/91JB00275.

Montési, L., & Hirth, G. (2003). Grain size evolution and the rheology of ductile shear zones: From laboratory experiments to postseismic creep. *Earth and Planetary Science Letters, 211*(1–2), 97–110. https://doi.org/10.1016/S0012-821X(03)00196-1.

Moreno, M., Melnick, D., Rosenau, M., Baez, J., Klotz, J., Oncken, O., et al. (2012). Toward understanding tectonic control on the M_w 8.8 2010 Maule Chile earthquake. *Earth and Planetary Science Letters, 321–322,* 152–165. https://doi.org/10.1016/j.epsl.2012.01.006.

Moreno, M., Rosenau, M., & Oncken, O. (2010). 2010 Maule earthquake slip correlates with pre-seismic locking of Andean subduction zone. *Nature, 467*(7312), 198–202.

Muto, J., Shibazaki, B., Iinuma, T., Ito, Y., Ohta, Y., Miura, S., et al. (2016). Heterogeneous rheology controlled postseismic deformation of the 2011 Tohoku-Oki earthquake. *Geophysical Research Letters, 43*(10), 4971–4978. https://doi.org/10.1002/2016GL068113.

Noda, A., Takahama, T., Kawasato, T., & Matsu'ura, M. (2017). Interpretation of offshore crustal movements following the 2011 Tohoku-Oki earthquake by the combined effect of afterslip and viscoelastic stress relaxation. *Pure and Applied Geophysics, 175*(2), 559–572.

Oleskevich, D., Hyndman, R., & Wang, K. (1999). The updip and downdip limits to great subduction earthquakes: Thermal and structural models of Cascadia, south Alaska, SW Japan, and Chile. *Journal of Geophysical Research Solid Earth, 104*(B7), 14965–14991. https://doi.org/10.1029/1999JB900060.

Perfettini, H., Avouac, J.-P., Tavera, H., Kositsky, A., Nocquet, J.-M., Bondoux, F., et al. (2010). Seismic and aseismic slip on the central Peru megathrust. *Nature, 465*(7294), 78–81. https://doi.org/10.1038/nature09062.

Pollitz, F. F., Bürgmann, R., & Banerjee, P. (2006). Post-seismic relaxation following the great 2004 Sumatra–Andaman earthquake on a compressible self-gravitating Earth. *Geophysical Journal International, 167,* 397–420. https://doi.org/10.1111/j.1365-246X.2006.03018.x.

Qiu, Q., Moore, J. D. P., Barbot, S., Feng, L., & Hill, E. M. (2018). Transient rheology of the Sumatran mantle wedge revealed by a decade of great earthquakes. *Nature Communications, 9,* 995. https://doi.org/10.1038/s41467-018-03298-6.

Ranalli, G. (1997). Rheology and deep tectonics. *Annali di Geofisica XL, 3,* 671–780. https://doi.org/10.4401/ag-3893.

Remy, D., Perfettini, H., Cotte, N., Avouac, J. P., Chlieh, M., Bondoux, F., et al. (2016). Postseismic relocking of the subduction megathrust following the 2007 Pisco, Peru, earthquake. *Journal of Geophysical Research Solid Earth, 121,* 3978–3995. https://doi.org/10.1002/2015JB012417.

Rundle, J. B. (1978). Viscoelastic crustal deformation by finite quasi-static sources. *Journal of Geophysical Research, 83*(B12), 5937–5946. https://doi.org/10.1029/JB083iB12p05937.

Scholz, C. (1998). Earthquakes and friction laws. *Nature, 391*(6662), 37–42.

Schurr, B., Asch, G., Hainzl, S., Bedford, J., Hoechner, A., Palo, M., et al. (2014). Gradual unlocking of plate boundary controlled initiation of the 2014 Iquique earthquake. *Nature, 512*(7514), 299–302. https://doi.org/10.1038/nature13681.

Springer, M. (1999). Interpretation of heat-flow density in the central Andes. *Tectonophysics, 306*(3), 377–395. https://doi.org/10.1016/S0040-1951(99)00067-0.

Sun, T., & Wang, K. (2015). Viscoelastic relaxation following subduction earthquakes and its effects on afterslip determination. *Journal of Geophysical Research Solid Earth, 120,* 1329–1344. https://doi.org/10.1002/2014JB011707.

Sun, T., Wang, K., Iinuma, T., Hino, R., He, J., Fujimoto, H., et al. (2014). Prevalence of viscoelastic relaxation after the 2011 Tohoku-Oki earthquake. *Nature, 514*(7520), 84–87. https://doi.org/10.1038/nature13778.

Takeuchi, C. S., & Fialko, Y. (2013). On the effects of thermally weakened ductile shear zones on postseismic deformation. *Journal of Geophysical Research Solid Earth, 118*(12), 6295–6310. https://doi.org/10.1002/2013JB010215.

Tichelaar, B. W., & Ruff, L. J. (1993). Depth of seismic coupling along subduction zones. *Journal of Geophysical Research, 98*(B2), 2017–2037. https://doi.org/10.1029/92JB02045.

Tsang, L. L. H., Hill, E. M., Barbot, S., Qiu, Q., Feng, L., Hermawan, I., et al. (2016). Afterslip following the 2007 M_w 8.4 Bengkulu earthquake in Sumatra loaded the 2010 M_w 7.8 Mentawai tsunami earthquake rupture zone. *Journal of Geophysical Research Solid Earth, 121,* 9034–9049. https://doi.org/10.1002/2016JB013432.

Vigny, C., Socquet, A., Peyrat, S., Ruegg, J.-C., Métois, M., Madariaga, R., et al. (2011). The M_w 8.8 Maule megathrust earthquake of central Chile, monitored by GPS. *Science, 332,* 1417–1421. https://doi.org/10.1126/science.1204132.

Völker, D., Grevemeyer, I., Stipp, M., Wang, K., & He, J. (2011). Thermal control of the seismogenic zone of southern central Chile. *Journal of Geophysical Research*. https://doi.org/10.1029/2011JB008247.

Wang, K., & Fialko, Y. (2014). Space geodetic observations and models of postseismic deformation due to the 2005 M7.6 Kashmir (Pakistan) earthquake. *Journal of Geophysical Research*

Solid Earth, 119(9), 7306–7318. https://doi.org/10.1002/2014JB011122.

Wang, K., & Fialko, Y. (2018). Observations and modeling of coseismic and postseismic deformation due to the 2015 M_w 7.8 Gorkha (Nepal) earthquake. *Journal of Geophysical Research Solid Earth, 123*(1), 761–779. https://doi.org/10.1002/2017JB014620.

Wang, K., Hu, Y., & He, J. (2012). Deformation cycles of subduction earthquakes in a viscoelastic Earth. *Nature, 484*(7394), 327–332. https://doi.org/10.1038/nature11032.

Yamagiwa, S., Miyazaki, S., Hirahara, K., & Fukahata, Y. (2015). Afterslip and viscoelastic relaxation following the 2011 Tohoku-oki earthquake (M_w 9.0) inferred from inland GPS and seafloor GPS/Acoustic data. *Geophysical Research Letters, 42*(1), 66–73. https://doi.org/10.1002/2014GL061735.

Yue, H., Lay, T., Rivera, L., An, C., Vigny, C., Tong, X., & Báez Soto, J.C. (2014). Localized fault slip to the trench in the 2010 Maule, Chile Mw = 8.8 earthquake. from joint inversion of high-rate GPS, teleseismic body waves, InSAR, campaign GPS, and tsunami observations. *J. Geophys. Res. Solid Earth*, *119*, 7786–7804. https://doi.org/10.1002/2014JB011340.

Zhao, B., Bürgmann, R., Wang, D., Tan, K., Du, R., & Zhang, R. (2017). Dominant Controls of Downdip Afterslip and Viscous Relaxation on the Postseismic Displacements Following the M_w 7.9 Gorkha, Nepal, Earthquake. *Journal of Geophysical Research Solid Earth, 122*(10), 8376–8401. https://doi.org/10.1002/2017JB014366.

(Received July 25, 2018, revised November 2, 2018, accepted December 29, 2018)